Open-Circuit Fault Identification Method for Interleaved Converters Based on Time-Domain Analysis of the State Observer Residual

Nicolas Wassinger, Emiliano Penovi, Rogelio Garcia Retegui, and Sebastian Maestri

***Abstract*—Fault-tolerance capability is a critical matter in power conversion systems that require continuous operation. Multiphase converters provide an inherent redundancy that gives them fault-tolerant capability. In addition, the interleaved operation of these converters provides them with some advantages regarding total current ripple, which otherwise would be lost under a fault condition. This issue can be solved by means of an identification and reconfiguration system. This paper proposes a method for open-circuit fault identification, based on the time-domain comparison of the residual of a state-space observer with signatures per phase. Signature online generation, together with a proper normalization and thresholding strategy, provides immunity with respect to the operation point. The use of the phase information associated to the interleaved operation allows to reduce the number of sensed variables, making it possible to identify the faulty leg by only sensing input and output signals, which are conventionally used for control purposes. Hence, the measurement of signals within every leg is avoided. Experimental results on a four-phase interleaved buck converter validate the method capacity to identify faults in two switching periods. Robustness regarding abrupt changes in the operational conditions was tested.**

***Index Terms*—Fault identification, fault-tolerant system, interleaved converter, signature-based identification, state observer.**

I. Introduction

MULTIPHASE power converters have become a power conversion scheme widely used in applications as diverse as electrical vehicles, renewable energy sources, and particle accelerator sources, among others [1]–[4]. These converters can efficiently operate high currents, since the total current is divided between their N phases. This feature reduces the requirements on semiconductor devices, which leads to efficiency improvement and a reduction of the converter size [5], [6]. Additionally, by means of an appropriate interleaving of phase current ripples, a reduction in the total current ripple amplitude and an increase in its frequency can be attained. These characteristics reduce the requirements of an associated filtering stage [7].

Another advantage of these converters is the possibility of operating even after a converter phase goes out of service. This characteristic is central to the above-mentioned applications, as the scenario of a converter going out of service is critical or has a strong economic impact. Nonetheless, phase failure leads to an increase in the current of the remaining phases and to an incorrect interleaving of phase current ripples. The former could be overcome by oversizing the converter components, while the latter increases the total current ripple due to the existence of a fundamental frequency component. This condition may imply operating the converter beyond the design specifications [8], [9].

As mentioned in the literature, the most common causes of faults can be explained by issues related to semiconductor devices [10], such as incorrect gate voltage, driver failure, lifting of bonding wires due to thermal cycling, or electrical overstress (i.e., voltage or current) [11], [12]. These faults can be broadly classified into short-circuit faults (SCFs) and open-circuit faults (OCFs). Even though SCF detection is crucial for system protection, SCF can turn into OCF if a fast hardware protection (like fuses) acts before the damage is spread along the system [10]. As a result, assuming that the system is hardware-protected against SCFs, only OCFs are considered in this paper.

The use of a detection and identification method would allow to determine the faulty phase, and could be further used to improve operating conditions, for instance, by relieving the damaged phase by means of an auxiliary one or by reconfiguring the control in order to adjust the phase shift among the remaining phases [12], [13]. However, in order to comply with the requirements of the mentioned applications, the identification method is expected to meet the following specifications.

1) Fast identification times, in the order of a few switching periods, so as to avoid the converter going out of service.
2) Reduced number of measurements, ideally only those used by the control algorithm, which is important for cost-constrained applications that employ current control techniques to avoid sensing every phase current [14]–[18].
3) Robustness against noise, especially when measurements that inherently contain commutation noise are used for fault identification.

Manuscript received December 29, 2017; revised March 9, 2018, April 19, 2018, and June 22, 2018; accepted June 29, 2018. Date of publication July 4, 2018; date of current version February 20, 2019. This work was supported in part by the National Scientific and Technical Research Council, in part by Universidad Nacional de Mar del Plata, in part by Argentine Ministry of Science, Technology and Productive Innovation, and in part by Argentine National Agency for Scientific and Technologic Promotion. Recommended for publication by Associate Editor A. Davoudi. *(Corresponding author: Nicolas Wassinger.)*

The authors are with the Instrumentation and Control Laboratory (LIC), Institute of Scientific and Technological Research in Electronics (ICYTE), Universidad Nacional de Mar del Plata (UNMDP), National Scientific and Technical Research Council (CONICET), Buenos Aires 7600, Argentina (e-mail: nwassinger@fi.mdp.edu.ar; emilianopenovi@fi.mdp.edu.ar; rgarcia@fi.mdp.edu.ar; somaestri@fi.mdp.edu.ar).

Color versions of one or more of the figures in this paper are available online at http://ieeexplore.ieee.org.

Digital Object Identifier 10.1109/TPEL.2018.2853574

4) Tolerance to converter parameter variability, which could be associated to passive component tolerance, aging, and temperature dependence, among other issues.
5) Robustness against changes on the operating point, related to the wide operating range in terms of input/output voltage, reference, and load of the power converters.
6) Capacity of tolerating changes in the number of phases, associated to reconfiguration algorithms or maximum efficiency control strategies that dynamically adjust the number of active phases [19].

In this regard, several research works dealing with fault detection and identification have been applied to power converters, such as a fast power switch fault detection algorithm based on Park's vector approach [10], a method based on computing dc-link current derivative sign variations [8], a method based on fast Fourier transform of the magnetic near-field of dc–dc converters [20], a method using circuit variable behavior [11], and fault identification methods based on the analysis of the residual present in the error vector of a state observer [13], [21]–[26]. These methods can be classified into two categories: those suitable for interleaved converters and those designed for such structures. The former have shown good performance in several applications, although their use on interleaved converters could present certain limitations, such as excessive identification times of the order of several commutation periods [23]–[25] or the requirement of further measurements, other than those used by the control algorithm [10], [11], [20]–[22]. Regarding the methods devised for interleaved applications, a method that only requires to measure the total current was proposed in [8], where tests results show identification times shorter than two commutation periods. However, its implementation strongly depends on the number of phases. Consequently, this method lacks of the flexibility required when operating under changes in the number of active phases. This drawback is not present in the residual-based identification systems, since the state observer correctly models the physical system regardless the number of active phases. In this methodology, the evolution of the system variables is evaluated and compared to their expected evolution under fault or normal operating conditions. Thus, the difference between the converter measured variables and those resulting from computing an analytical model, i.e., the output error vector, includes the so-called residual, which is representative of the mismatches between fault-less and faulty models. On the other hand, possible slow drifts in the residual generated by the imperfect knowledge of the model parameters or the effects of disturbances and noise can be compensated by a proper adjustment of the state observer gains. Thus, the residual remains bounded in the absence of faults, while providing enough information for fault detection, if the observer is properly tuned. In [13], a general method capable of identifying faults in different types of components in interleaved converters was presented. In spite of its good performance, it requires all phase currents to be measured, and it takes a few tens of commutation periods to identify the faults. However, residual-based identification methods offer a good balance among simplicity, robustness, and low-computational resources [27], rendering it attractive for identification in interleaved systems.

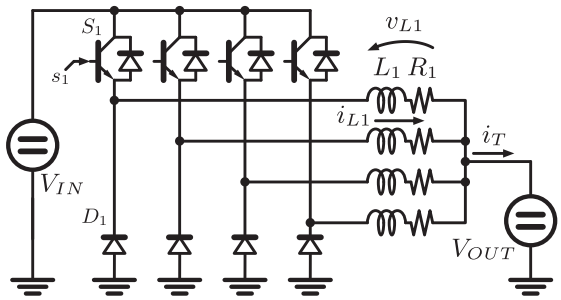

Fig. 1. Four-phase interleaved buck converter.

This paper presents a fault identification strategy based on the residual analysis of a state observer, which uses the phase information of the total current inherent to the interleaved operation of these converters. This proposal allows to identify the faulty phase with a reduced number of sensed variables and low-computational resources. The proposed algorithm is used to identify OCF in multiphase dc–dc converters, and only requires the measurement of variables commonly employed for the control schemes (input and output dc-link voltage and total current). This paper is organized as follows. Section II introduces the theoretical framework related to the system modeling under normal and fault operation together with the state observer design. Section III presents the proposed algorithm and describes the implementation features. The experimental setup, comprising a four-phase multiphase buck converter, along with the experimental results is presented in Section IV. Finally, Section V draws the main conclusions of this paper.

II. Theoretical Framework for Residual Analysis

This section presents the theoretical framework adopted to analyze OCF on interleaved converters, together with the relevant notation and terminology. First, the state-space system model for nonfault and fault cases is described, then the state observer to generate the residual is presented, and finally, the residual is analyzed for each considered fault. A four-phase interleaved buck converter, shown in Fig. 1, is presented as an illustrating example of the proposal. Each leg is composed of a diode D_n, that works as a natural commutation device, and a controlled switch, S_n, being s_n the command signal. L_n is the leg inductance, and R_n its associated resistance, where i_{Ln} and v_{Ln}, respectively, indicate the inductor current and voltage. Total current, i_T, results from the sum of the inductor currents, i.e., $i_T = \sum i_{Ln}$.

Throughout the analysis, input and output voltages, V_{IN} and V_{OUT}, are considered constant within a commutation period. Additionally, continuous conduction mode operation is assumed on steady state, so noncontrolled and controlled switch states result complementary in the nonfault condition. Then, only two topological states are allowed for each leg, the ON state when $s_n = 1$, and the OFF state when $s_n = 0$.

A. System Model

Switching power converters can be described as a continuous-time system with discrete switching events. In general, their

dynamics can be defined by a linear-switched state-space model of the form [28]

$$\dot{\mathbf{x}}(t) = \mathbf{A}_{\sigma(t)}\mathbf{x}(t) + \mathbf{B}_{\sigma(t)}\mathbf{u}(t) \tag{1}$$

$$\mathbf{y}(t) = \mathbf{C}\mathbf{x}(t) \tag{2}$$

where $\mathbf{x}(t)$ is the vector of state variables, $\mathbf{u}(t)$ is the vector of system inputs, and $\mathbf{y}(t)$ is the vector of system outputs; $\mathbf{A}_{\sigma(t)}$, $\mathbf{B}_{\sigma(t)}$, and $\mathbf{C}$ are the set of state matrices for each linear state-space, where $\sigma(t)$ is an index associated to a finite set of values given by any valid combination of command signal states $[s_1\ s_2 \cdots\ s_N]$, which represents the active model at any time.

For the presented interleaved example, by defining $\mathbf{u}(t) = [V_{\text{IN}}\ V_{\text{OUT}}]^T$, $\mathbf{y}(t) = [i_T(t)]$ and $\mathbf{x}(t) = [i_{L1}(t)\quad i_{L2}(t)\ i_{L3}(t)\quad i_{L4}(t)]^T$, the state matrices results in the following:

$$\mathbf{A}_{\sigma(t)} = \begin{bmatrix} -R_1/L_1 & 0 & 0 & 0 \\ 0 & -R_2/L_2 & 0 & 0 \\ 0 & 0 & -R_3/L_3 & 0 \\ 0 & 0 & 0 & -R_4/L_4 \end{bmatrix} \tag{3}$$

$$\mathbf{B}_{\sigma(t)} = \begin{bmatrix} s_1(t)/L_1 & -1/L_1 \\ s_2(t)/L_2 & -1/L_2 \\ s_3(t)/L_3 & -1/L_3 \\ s_4(t)/L_4 & -1/L_4 \end{bmatrix} \tag{4}$$

$$\mathbf{C} = \begin{bmatrix} 1 & 1 & 1 & 1 \end{bmatrix}. \tag{5}$$

Considering that the system model is defined by the converter components and its topology, the occurrence of a fault causes $\mathbf{A}_{\sigma(t)}$ and $\mathbf{B}_{\sigma(t)}$ matrices to change. Then, under this condition, the converter is modeled with a new set of matrices, named $\tilde{\mathbf{A}}_{\sigma(t)}$ and $\tilde{\mathbf{B}}_{\sigma(t)}$. As a consequence, it is possible to represent the effect of a fault on the system by means of deviation matrices, $\Delta\mathbf{A}_{\sigma(t)}$ and $\Delta\mathbf{B}_{\sigma(t)}$, which are defined as the difference between the state matrices for the cases with and without faults

$$\Delta\mathbf{A}_{\sigma(t)} \triangleq \tilde{\mathbf{A}}_{\sigma(t)} - \mathbf{A}_{\sigma(t)} \tag{6}$$

$$\Delta\mathbf{B}_{\sigma(t)} \triangleq \tilde{\mathbf{B}}_{\sigma(t)} - \mathbf{B}_{\sigma(t)}. \tag{7}$$

Then, the equation for the state-space model results in

$$\dot{\mathbf{x}}(t) = (\mathbf{A}_{\sigma(t)} + \Delta\mathbf{A}_{\sigma(t)})\mathbf{x}(t) + (\mathbf{B}_{\sigma(t)} + \Delta\mathbf{B}_{\sigma(t)})\mathbf{u}(t). \tag{8}$$

Following the example, the deviation matrices when an OCF in phase 1 is considered result in

$$\Delta\mathbf{A}_{\sigma(t)} = 0 \tag{9}$$

$$\Delta\mathbf{B}_{\sigma(t)} = \begin{bmatrix} -s_1(t)/L_1 & 0 \\ 0 & 0 \\ 0 & 0 \\ 0 & 0 \end{bmatrix}. \tag{10}$$

Then, (11) results from rewriting (8) as the sum of the nonfault case model equation and a term associated to the fault, $\mathbf{g}_f\phi_f(t)$

$$\dot{\mathbf{x}}(t) = \mathbf{A}_{\sigma(t)}\mathbf{x}(t) + \mathbf{B}_{\sigma(t)}\mathbf{u}(t) + \mathbf{g}_f\phi_f(t) \tag{11}$$

$$\mathbf{g}_f\phi_f(t) = \Delta\mathbf{A}_{\sigma(t)}\mathbf{x}(t) + \Delta\mathbf{B}_{\sigma(t)}\mathbf{u}(t) \tag{12}$$

TABLE I
HEALTH STATE IDENTIFIERS

f	Health state	$\phi_f(t)$	$\mathbf{g}_f$	$\mathbf{C}\mathbf{g}_f$
0	non-fault	0	$[0\ 0\ 0\ 0]^T$	[0]
1	S_1 fault	- $s_1(t)\frac{V_{IN}}{L_1}$	$[1\ 0\ 0\ 0]^T$	[1]
2	S_2 fault	- $s_2(t)\frac{V_{IN}}{L_2}$	$[0\ 1\ 0\ 0]^T$	[1]
3	S_3 fault	- $s_3(t)\frac{V_{IN}}{L_3}$	$[0\ 0\ 1\ 0]^T$	[1]
4	S_4 fault	- $s_4(t)\frac{V_{IN}}{L_4}$	$[0\ 0\ 0\ 1]^T$	[1]

where $f \in \{0, 1, \ldots, F\}$ is an index that identifies the health state of the converter, F is the number of considered faults and $f = 0$ corresponds to the nonfault condition. $\mathbf{g}_f$ and $\phi_f(t)$ are defined so that $\mathbf{g}_f$ results in a time invariant vector, while $\phi_f(t)$ results in a scalar term that models the dynamic evolution after a fault event. Taking into account that the faults considered in this paper correspond to an OCF in each phase, the number of possible faults, F, equals the number of phases, N. For the case under analysis, Table I presents the values adopted by $\phi_f(t)$ and $\mathbf{g}_f$ for each possible f.

B. Observer-Based Residual

Equations (13) and (14) describe a state observer for the faultless system model given by (1) and (2) as

$$\dot{\hat{\mathbf{x}}}(t) = \mathbf{A}_{\sigma(t)}\hat{\mathbf{x}}(t) + \mathbf{B}_{\sigma(t)}\mathbf{u}(t) - \mathbf{H}\boldsymbol{\gamma}(t) \tag{13}$$

$$\boldsymbol{\gamma}(t) = \mathbf{C}\hat{\mathbf{x}}(t) - \mathbf{y}(t) \tag{14}$$

where $\hat{\mathbf{x}}(t)$ is the vector of the observer state variables, $\mathbf{H} = [h_1 h_2 \cdots h_N]^T$ is the observer gain vector, and $\boldsymbol{\gamma}(t)$ is the difference between estimated and measured outputs.

In view of the fact that the converter could operate under a fault condition, the state-space model of the converter is given by (11). Accordingly, operating with (11)–(14), the equations associated with the observer error in the state variables, $\mathbf{e}(t) \triangleq \hat{\mathbf{x}}(t) - \mathbf{x}(t)$, and the difference between the estimated and measured outputs are obtained as follows:

$$\dot{\mathbf{e}}(t) = \left(\mathbf{A}_{\sigma(t)} - \mathbf{H}\mathbf{C}\right)\mathbf{e}(t) - \mathbf{g}_f\phi_f(t) \tag{15}$$

$$\boldsymbol{\gamma}(t) = \mathbf{C}\mathbf{e}(t). \tag{16}$$

From (15) and (16), (17) can be obtained, which models the time evolution of the output error

$$\boldsymbol{\gamma}(t) = \mathbf{C}e^{-\left(\mathbf{A}_{\sigma(t)} - \mathbf{H}\mathbf{C}\right)t}\mathbf{e}(0) + \mathbf{C}\mathbf{g}_f \int_0^t \phi_f(t)\, e^{-\left(\mathbf{A}_{\sigma(t)} - \mathbf{H}\mathbf{C}\right)(t-\tau)} d\tau. \tag{17}$$

$\mathbf{C}e^{-\left(\mathbf{A}_{\sigma(t)} - \mathbf{H}\mathbf{C}\right)t}\mathbf{e}(0)$ term is the system response to the initial condition, $\mathbf{e}(0)$, which decays to zero in steady-state condition. Then, in steady state, the residual results in

$$\boldsymbol{\gamma}(t) = \mathbf{C}\mathbf{g}_f \int_0^t \phi_f(t)\, e^{-\left(\mathbf{A}_{\sigma(t)} - \mathbf{H}\mathbf{C}\right)(t-\tau)} d\tau. \tag{18}$$

It is worth highlighting that $\mathbf{C}\mathbf{g}_f$ defines the components of the output error vector given by $\gamma(t)$ that are affected by

the occurrence of a failure. This term can be interpreted as the residual direction defined by the components of the output vector space. Therefore, if enough variables are measured, the residual direction would allow to identify a fault among multiple possible causes [13], [21]. However, in multiphase converters in which measurements of phase variables are avoided, the output error vector only has one component (total current). Consequently, the analysis of the residual direction alone would allow to detect the fault. Yet this analysis does not provide sufficient information for its identification. This condition can be observed in Table I, where the use of only one measured variable defines that $\mathbf{Cg}_f$ has only one component, which presents the same value for all possible fault cases. In spite of this, it can be observed from (18) that the output error has time information arising from the term $\phi_f(t)$ affected by the transfer function associated to the eigenvalues of $\left(\mathbf{A}_{\sigma(t)} - \mathbf{HC}\right)$, which can be used to identify faults.

III. Proposed Fault Identification Method

This paper proposes an identification method that makes use of the total current measurement to identify OCFs in each phase, by using phase shift information present in this signal inherent to the interleaved operation. In this operating mode, $\phi_f(t)$ and, by extension, $\boldsymbol{\gamma}(t)$ contain fault temporal information additional to the $\mathbf{Cg}_f$ direction information, that allows to univocally identify the faulty phase. In other words, $\boldsymbol{\gamma}(t)$ differs in each particular fault. Then, the proposed method consists in computing the expected evolutions of the residual $\boldsymbol{\gamma}(t)$ for each fault to be identified and using them as fault signatures, called $\boldsymbol{\gamma}_f^*(t)$. Fig. 2 illustrate the waveforms associated to the example case. The fault signatures shown in Fig. 2(b) are filtered versions with changed sign of the command signals shown in Fig. 2(a), as it can be seen by analyzing (18) with Table I data. If an OCF in phase 1 is considered again, the phase currents are the ones shown in Fig. 2(c), where, after a fault event, i_{L1} begins to fall even if the command signal is still ON. The residual signal is shown in Fig. 2(d), which remains equal to zero before the fault event. From the moment the fault occurs, the residual $\gamma(t)$ becomes similar to the fault signature corresponding to the faulty phase, $\gamma_1^*(t)$. Based on this, the generation of signals whose value allows to measure the similarity between each fault signature and the residual, named $\mathrm{IP}_f(t)$, is proposed along with the identification of faulty phases when any of such similarity signals reaches a threshold.

In order to represent the instantaneous health state of the physical system, the f_{PS} variable is defined. Then, when there is no fault, f_{PS} adopts the value zero. Conversely, when a fault occurs, it adopts a value that identifies such fault. Based on the example under study, in which an OCF in phase 1 is considered, f_{PS} results equal to the number of the faulty phase ($f_{PS} = 1$). When the fault occurs, the residual will present the same phase shift as the fault signature associated to such fault. Consequently, the similarity signal associated to the faulty phase, $\mathrm{IP}_{f_{PS}}$, will always result higher than any of the similarity signals associated to the healthy phases.

A block diagram of the proposed identification system is shown in Fig. 3. This scheme comprises the following:

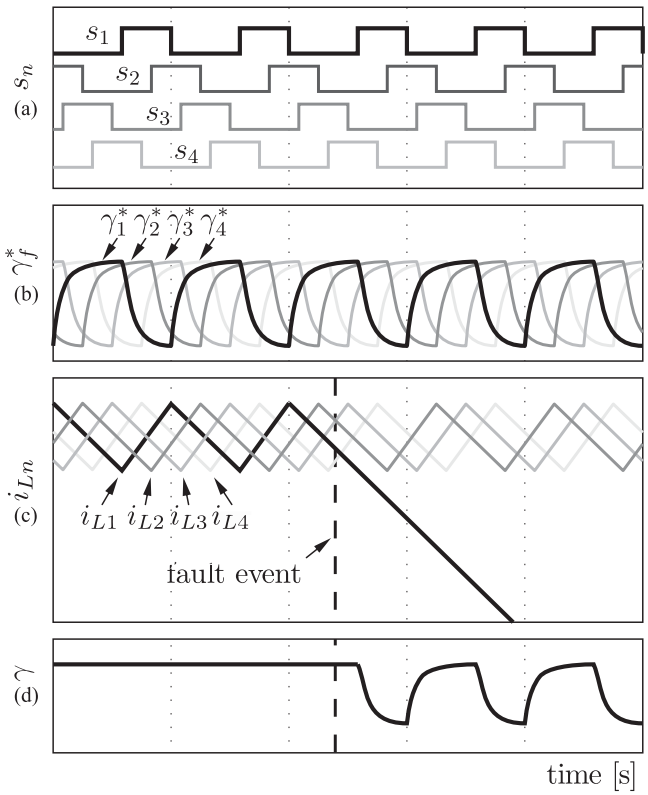

Fig. 2. System signals during a fault event. (a) Command signals. (b) Fault signatures. (c) Phase currents. (d) Residual.

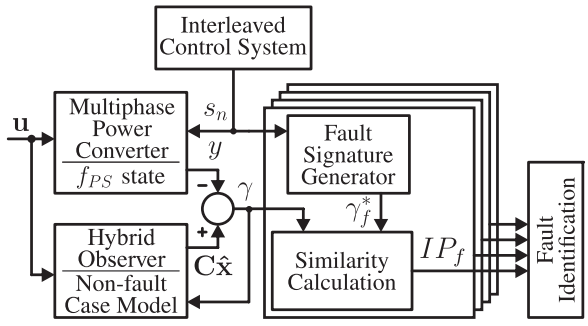

Fig. 3. Block diagram of the identification algorithm.

1) A power converter (that could be either on fault condition or not) and a nonfault case observer, whose outputs make up the residual $\gamma(t)$.
2) A control system, intended to generate switch command signals.
3) F fault signature generator blocks, that obtain the phase shift information from the switch command signals.
4) F similarity calculation blocks, that provide $\mathrm{IP}_f(t)$ signals indicative of the similarity between fault signatures and the residual.
5) The fault identification block used to establish the fault cause from the similarity signal information.

A. Fault Signatures

The OCF fault considered in this paper occurs when a switch remains open when its command signal is in ON state.

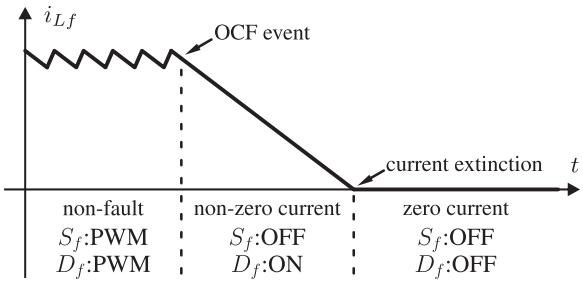

Fig. 4. System evolution after OCF event in phase f (nonfault, nonzero current, and zero current stages).

Fig. 4 illustrates the evolution of the faulty phase current in the case of an OCF fault in phase f. A fault event begins when the switch S_f loses its capability of driving current. Initially, the D_f diode remains ON until the L_f inductor current is extinguished. Then, both controlled switch and diode have zero current. These stages are denoted in Fig. 4 as nonfault, nonzero current, and zero current.

The absence of the faulty phase current in the zero current stage produces modifications in the fault signatures indicated in Table I. The new values can be calculated following the same procedure as for the nonzero current stage; in this case, $\mathbf{g}_f$ turns out to remain equal, while $\phi_f(t)$ changes from $\phi_f(t) = -s_f(t)\frac{V_{\text{IN}}}{L_f}$ to $\phi_f(t) = -s_f(t)\frac{V_{\text{IN}}}{L_f} + \frac{V_{\text{OUT}}}{L_f}$, i.e., only its mean value, $\langle\phi_f(t)\rangle$, is modified. Note that the signal obtained when removing the mean value of $\phi_f(t)$ keeps the time information useful for fault identification. Hence, in order to use just one fault signature regardless of the stage under analysis, fault signatures are computed by subtracting mean values from $\phi_f(t)$ signals and applying the dynamic response of the system

$$\boldsymbol{\gamma}_f^*(t) = \mathbf{C}\mathbf{g}_f \int_0^t \left(\phi_f(t) - \langle\phi_f(t)\rangle\right) e^{-\left(\mathbf{A}_{\sigma(t)} - \mathbf{H}\mathbf{C}\right)(t-\tau)} d\tau \tag{19}$$

where $h_1 = h_2 = \cdots = h_N = h$ is adopted. Equation (19) corresponds to a low-pass filter for the topology covered by this paper, whose cutoff frequency is mostly dependent on the observer gains if $h >> R/L$ is adopted, allowing to minimize algorithm dependence on converter parameters. Under this condition, the cutoff frequency and the low-frequency gain can be approximated by Nh and $1/h$, respectively. Then, the tradeoff between waveform distortion and signal-to-noise ratio must be considered when defining the h value, i.e., a large h results not only in a $\boldsymbol{\gamma}(t)$ waveform close to the command signal one, but also in a small $\boldsymbol{\gamma}(t)$ magnitude, leading to possible noise problems. On the other hand, a small h value would improve the noise filtering at the expense of higher distortion.

B. Similarity Signals

In order to obtain signals whose steady-state value represents only the similarity between residual and fault signature waveform and phase, a sliding window inner product is performed

$$\left\langle \boldsymbol{\gamma}, \boldsymbol{\gamma}_f^* \right\rangle (t) = \int_{t-W}^{t} \boldsymbol{\gamma}(\tau)\boldsymbol{\gamma}_f^*(\tau) d\tau \tag{20}$$

where W is the sliding window length.

Equation (20) can be rewritten as (21), where residual and fault signatures are represented by their mean values ($\langle\cdot\rangle$) and variations ($\tilde{\cdot}$)

$$\int_{t-W}^{t} \tilde{\boldsymbol{\gamma}}\,\tilde{\boldsymbol{\gamma}}_f^* d\tau + \left\langle \boldsymbol{\gamma}_f^* \right\rangle \int_{t-W}^{t} \left(\langle\boldsymbol{\gamma}\rangle + \tilde{\boldsymbol{\gamma}}\right) d\tau + \langle\boldsymbol{\gamma}\rangle \int_{t-W}^{t} \tilde{\boldsymbol{\gamma}}_f^* d\tau. \tag{21}$$

The first term of (21) contains the required similarity information. Provided that the fault signatures were designed to have a zero mean value, the second term would result null. Finally, the last term can be eliminated if the window length is adopted as an integer multiple of the commutation period, which is easily achievable if both identification and control algorithms are implemented in the same digital platform.

In view of the fact that the signatures only differ in their phase shift, a converter fault could lead to nonzero inner products even in faultless phases. Nonetheless, the highest inner product will be the one associated to the faulty phase, as expected. This value can be theoretically calculated as the steady-state level resulting from evaluating (20) when the signatures correspond to the fault case. Since the fault signatures only differ by their phase shift, such factor is the same regardless of the faulty phase. Hence, the highest inner product can be obtained by taking any fault signature, $\gamma^*(t)$, and calculating the inner product with itself, i.e., $\langle\boldsymbol{\gamma}^*, \boldsymbol{\gamma}^*\rangle(\infty)$. Then, fault identification can be achieved by tracking similarity signals and comparing them to a threshold, Γ, set to identify the faulty phase. For Γ to remain independent of the system parameters, the similarity signals are obtained by normalizing (20) by the highest inner product. Finally, similarity signals result in

$$\text{IP}_f(t) = \frac{\left\langle \boldsymbol{\gamma}, \boldsymbol{\gamma}_f^* \right\rangle (t)}{\langle \boldsymbol{\gamma}^*, \boldsymbol{\gamma}^* \rangle (\infty)}. \tag{22}$$

Fig. 5 shows similarity signals for the example case, considering an OCF event in phase 1. The residual and fault signatures are shown in Fig. 5(a) and (b), respectively. The variable $\Delta\varphi$ is defined in this figure, which corresponds to the relative phase shift among the residual $\gamma(t)$ and each fault signature $\gamma_f^*(t)$. Then, for the case of OCF in phase 1, $\Delta\varphi = 0$ determines that the phase shift between $\gamma(t)$ and $\gamma_1^*(t)$ is the same; hence, the inner product between the residual and such fault signature will be maximum. The similarity signals IP_f are displayed in Fig. 5(c), showing that all of them respond to the fault event with the same dynamics, but different steady-state values, $\text{IP}_f(\infty)$. It can be observed that the similarity signal associated to the faulty phase presents a steady-state value, $\text{IP}_1(\infty)$, which should be equal to 1 due to the normalization process, while the steady-state values of the healthy phases, $\text{IP}_2(\infty)$, $\text{IP}_3(\infty)$, and $\text{IP}_4(\infty)$, result lower than 1.

C. Thresholding

In order to properly define the threshold value, it is necessary to determine the range variation of $\text{IP}_f(\infty)$ for all possible operating conditions of the power converter. To obtain such a range variation, the values of $\text{IP}_f(\infty)$ are obtained using (22). Fig. 6 shows $\text{IP}_f(\infty)$ value as a function of $\Delta\varphi$, which can take values given by the phase shift interleaving, i.e., $\Delta\varphi$ will be

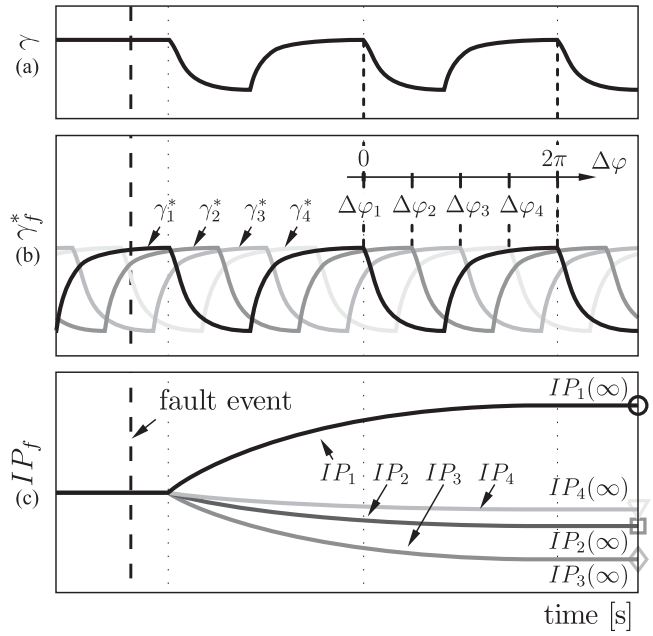

Fig. 5. Similarity definition. (a) Residual. (b) Fault signatures. (c) Similarity signals.

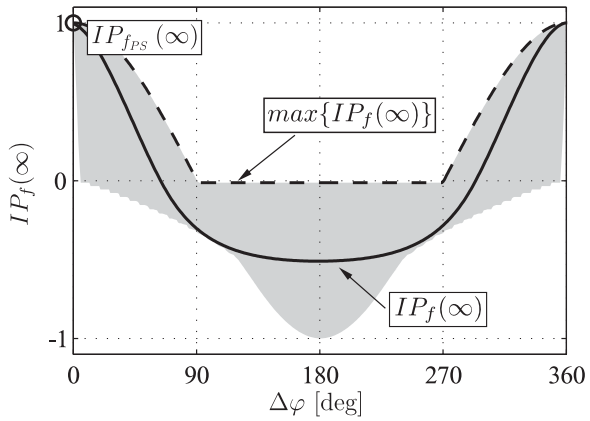

Fig. 6. Similarity signal steady-state values.

divided into 360°/N intervals. For the four-phase example, $\Delta\varphi$ results in 0°, 90°, 180°, and 270°.

It is worth considering that this curve varies with h and the duty cycle, D. In this sense, the figure shows the case of a particular combination of these parameters (solid line), together with a grey zone that corresponds to all curves for any available combination of h and D. Notice that, although $\Delta\varphi$ can only take N values, the grey zone is shown as continuous to take into account all possible values of N. In addition, the dashed curve is the envelope of maximum values of $\mathrm{IP}_f(\infty)$ for every combination of h and D, thereby, representing a worst case scenario with respect to identification. It is worth underlining that the relationship between $\mathrm{IP}_f(\infty)$ and the duty cycle results symmetrical to $D = 0.5$.

Noise and component value deviations, among other things, may cause $\mathrm{IP}_f(\infty)$ to vary, leading to possible uncertainty in fault identification. In order to mitigate this, the threshold is set at the midpoint between $\mathrm{IP}_f(\infty)$ for the faulty phase, which is always equal to 1, and the maximum value of the $\mathrm{IP}_f(\infty)$ associated to the faultless phases. The curve shape in Fig. 6 evidences that such value is obtained from the $\mathrm{IP}_f(\infty)$ nearest to $\mathrm{IP}_{f_{PS}}(\infty)$. Therefore, the threshold can be calculated as

$$\Gamma = (1 + \mathrm{IP}_{(f_{PS}+1)}(\infty))/2. \tag{23}$$

Table II lists the $\mathrm{IP}_{(f_{PS}+1)}(\infty)$ and Γ values for different N.

Finally, the fault identification block is in charge of tracking IP_f signals and identifying a fault event when the $\mathrm{IP}_{f_{PS}} > \Gamma$ condition is identified.

TABLE II
THRESHOLDS VALUES FOR DIFFERENT N

N	2	3	4	5	6	7	8	9
$\Delta\varphi$ intervals	180°	120°	90°	72°	60°	51.43°	45°	40°
$IP_{(f_{PS}+1)}(\infty)$	0	0	0	0.3	0.48	0.61	0.69	0.75
Γ	0.5	0.5	0.5	0.65	0.74	0.80	0.84	0.88

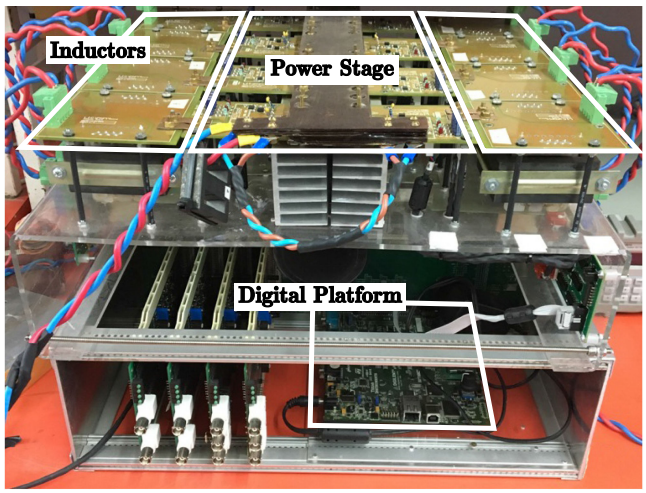

Fig. 7. Experimental setup: Four-phase interleaved buck converter.

IV. EXPERIMENTAL RESULTS

The proposed identification method was validated on a four-phase buck converter controlled by a digital platform. The main blocks are shown in Fig. 7, where the digital platform, the power stage, and the phase inductors are highlighted. The digital platform consist on an FPGA development board, the power stage is composed of four legs with fast 650 V 50 A IGBT switches, and the phase inductors were built using gapped EE cores (Mf102 ferrite Pryde E70/33/32). Additionally, 25 A Hall effect sensors (LEM LA25NP) were used for current measurement. In order to emulate OCF events, the command signal inhibiting capability was added to the control block. The main converter parameters are displayed in Table III. Variations of 10% with respect to the nominal values of the phase inductors and their associated resistive component were intentionally added to evaluate the method robustness against component tolerances. These nominal values, L_{nom} and R_{nom}, were the ones adopted for the identification algorithm adjustment.

The switch command signals and the total current were acquired using a MSO4034 oscilloscope together with a TCP303 current probe and the identification algorithm was computed in MATLAB/Simulink for simplicity reasons. As regards

TABLE III
EXPERIMENTAL SETUP SPECIFICATIONS

Input Voltage	V_{IN}	12 V −120 V
Output Voltage	V_{OUT}	5 V
Mean Output Current	$< I_T >$	12 A
Nominal Phase Inductance	L_{nom}	120 μH
Nominal Phase Resistance	R_{nom}	10 mΩ
IGBT modules		Infineon IKW50N65F5
Controller switching frequency	f_{sw}	25 kHz
Controller platform		Digilent Spartan 3E-1600
Estimator frequency	f_s	1.5 MHz
Estimator current sensor		Tektronix TCP 303

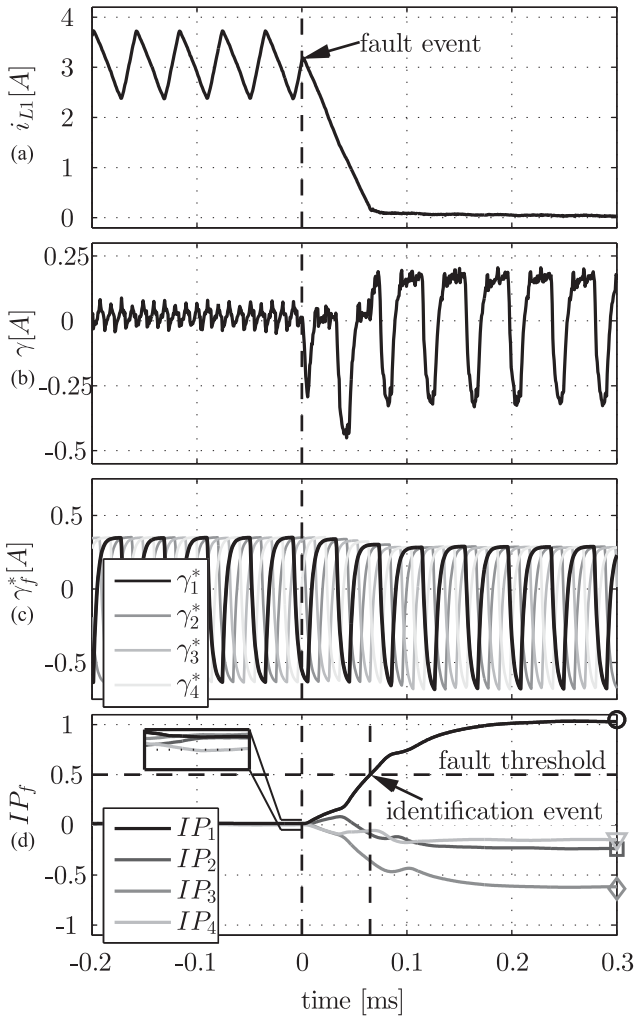

Fig. 8. Relevant signals evolution after a fault event ($D = 0.3$). (a) Faulty phase current. (b) Residual. (c) Fault signatures. (d) Similarity signals.

algorithm implementation, restrictions associated with conventional digital platforms, such as quantization, sample frequency, and finite word length, to name a few, were taken into account.

The test presented in this section can be divided into two types. To begin with, some tests emulating an OCF fault are presented and analyzed. Then, the robustness of the proposed algorithm against changes in the reference and the load is evaluated.

Fig. 8 depicts the algorithm performance after a fault event in phase 1 at $t = 0$. Faulty phase current i_{L1} is displayed in Fig. 8(a). As it can be seen, the fault event occurs in the middle of an ON period. The residual $\boldsymbol{\gamma}(t)$, which results from subtracting the measured total current from the estimated current, is depicted in Fig. 8(b). In turn, the $\boldsymbol{\gamma}_f^*(t)$ signatures for each OCF fault generated by filtering the switch command signals are displayed in Fig. 8(c). Filter bandwidth was selected as a function of the observer gain, and was equal to $Nh/2\pi \approx 45$ kHz. Before the OCF event, reduced magnitude variations occurred in $\boldsymbol{\gamma}(t)$ due to noise presence and phase ripple imbalances. On the other hand, after the fault event, the similarity in terms of waveform and phase shift between $\boldsymbol{\gamma}(t)$ and the signature associated with the emulated fault, $\boldsymbol{\gamma}_1^*(t)$, became evident.

Fig. 8(d) illustrates the inner products, $\text{IP}_f(t)$. The fault threshold was set for a four-phase system, i.e., $\Gamma = 0.5$ from Table II. The zoom in Fig. 8(d) shows that before the fault event, the value of the inner products was reduced and different from zero, due to modeling inaccuracies, among others. However, the proper fault threshold adjustment allowed to avoid false positives. After the fault event, $\text{IP}_f(t)$ evolved to their steady-state values, shown on the right-hand corner of the figure by means of different markers associated with each phase. The normalized inner product related to the faulty phase reached a value close to $\text{IP}_1(\infty) = 1$, which is in line with the designed normalization strategy, while the remaining ones were considerably lower, allowing to clearly identify the fault origin. Some variations are observed on the $\text{IP}_f(t)$ evolutions due to the transition of $i_{L1}(t)$ from nonzero current to zero current stages. Commutation frequency ripple results negligible as a consequence of the choice of a sliding window inner product.

The test presented in Fig. 8 was repeated for several D in order to evaluate identification times. It is worth noticing that, during the nonzero current stage, an OCF event becomes evident only when the corresponding switch command is ON, while the same behavior as in the faultless condition is maintained during the remaining commutation period. As a consequence, the time at which the fault occurs relative to the switching pattern of the faulty phase defines the identification time. If the fault event occurs at the beginning of an ON interval, the algorithm immediately obtains information from $\boldsymbol{\gamma}(t)$ and the identification time results minimum. Conversely, when the fault occurs at the beginning of an OFF interval, the algorithm only obtains information in the next turn ON command event. Based on the above, the worst case scenario for the identification time is obtained as the sum of the longest OFF period, i.e., one commutation cycle, and the maximum time taken from the beginning of an ON period to the identification event. In order to evaluate the latter, identification time tests were performed forcing the fault event to be synchronized to the beginning of an ON stage. Residual and similarity signals for $D = 0.1$ are shown in Fig. 9(a) and (b), for $D = 0.2$ in Fig. 9(c) and (d), for $D = 0.3$ in Fig. 9(e) and (f), and for $D = 0.4$ in Fig. 9(g) and (h). Only D values below 0.5 were evaluated due to the symmetry around this value. The identification times observed in Fig. 9 are close to a commutation cycle for all D, leading to a maximum identification time close to two switching periods. This correspondence demonstrates the independence between identification time and the duty cycle achieved by means of the normalization strategy.

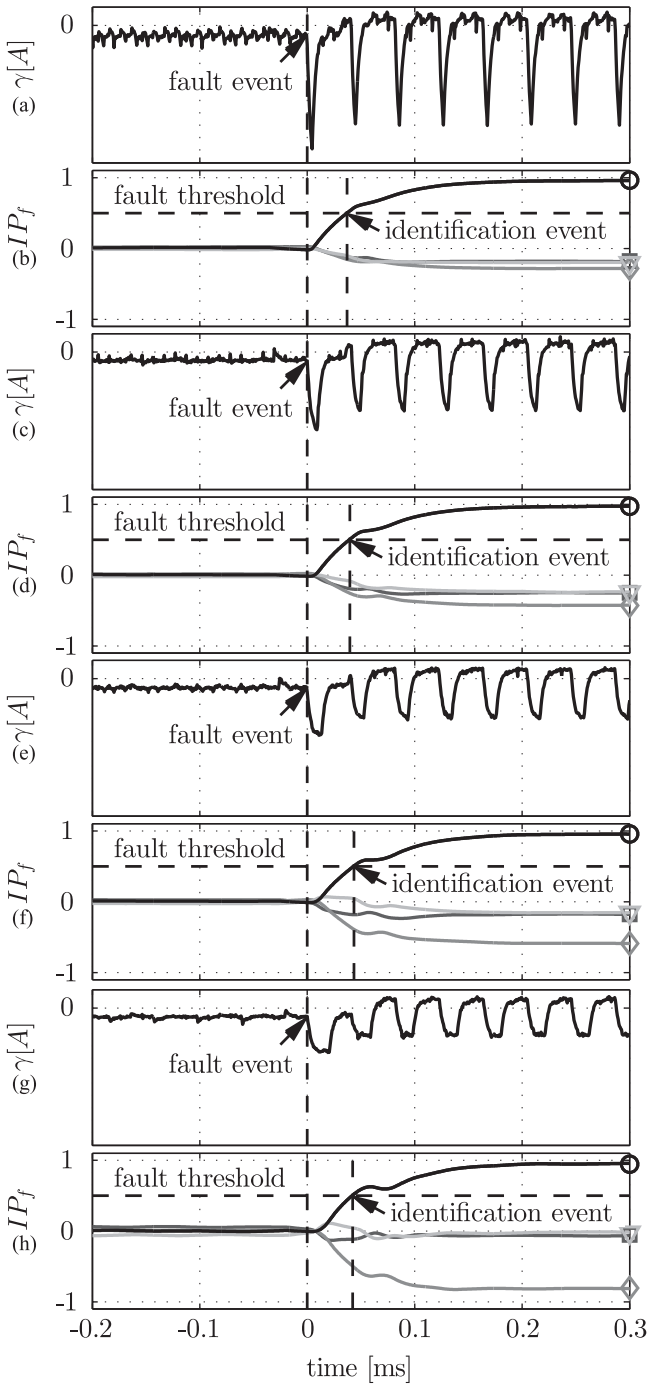

Fig. 9. Evaluation of identification time. Fault event synchronized to rising edge of s_1 signal. (a) and (b) $D = 0.1$. (c) and (d) $D = 0.2$. (e) and (f) $D = 0.3$. (g) and (h) $D = 0.4$.

Fig. 10 shows the theoretical solutions for several duty cycles (solid lines), together with the worst case scenario (dashed line) and the experimental results obtained from Fig. 9 (markers). Notice that the markers used for each phase are the same as those in Figs. 8 and 9. Experimental and theoretical values are also reported in Table IV, where the similarity between them is worth highlighting. Besides, all the $\mathrm{IP}_f(\infty)$ associated to the healthy phases remain below the worst case scenario predicted

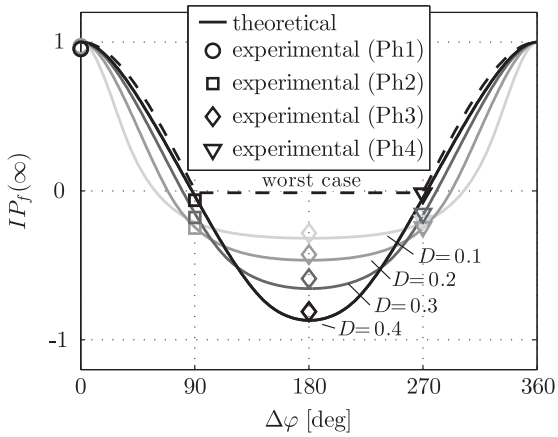

Fig. 10. Normalized inner products for different duty cycles. Analytical and experimental comparison. Markers correspond to four-phase case.

TABLE IV
EXPERIMENTAL AND THEORETICAL STEADY-STATE INNER PRODUCTS (THEORETICAL VALUES INDICATED BETWEEN BRACKETS)

D	$IP_1(\infty)$	$IP_2(\infty)$	$IP_3(\infty)$	$IP_4(\infty)$
0.1	0.96 (1)	-0.18 (-0.20)	-0.28 (-0.30)	-0.20 (-0.20)
0.2	0.97 (1)	-0.25 (-0.25)	-0.43 (-0.47)	-0.24 (-0.25)
0.3	0.96 (1)	-0.18 (-0.18)	-0.59 (-0.63)	-0.15 (-0.18)
0.4	0.95 (1)	-0.06 (-0.04)	-0.81 (-0.87)	-0.02 (-0.04)

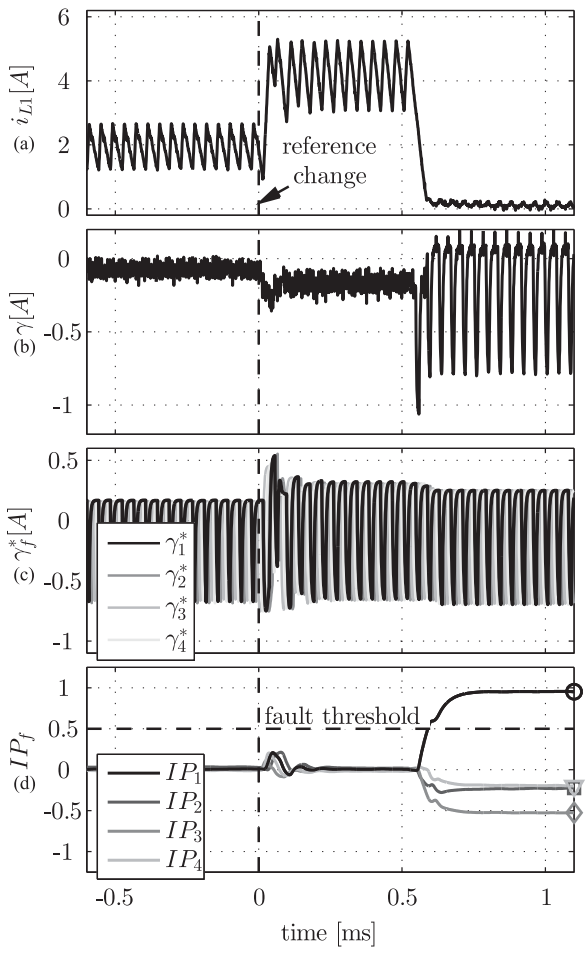

Fig. 11. Relevant signals evolution after a reference change. (a) Faulty phase current. (b) Residual. (c) Fault signatures. (d) Similarity signals.

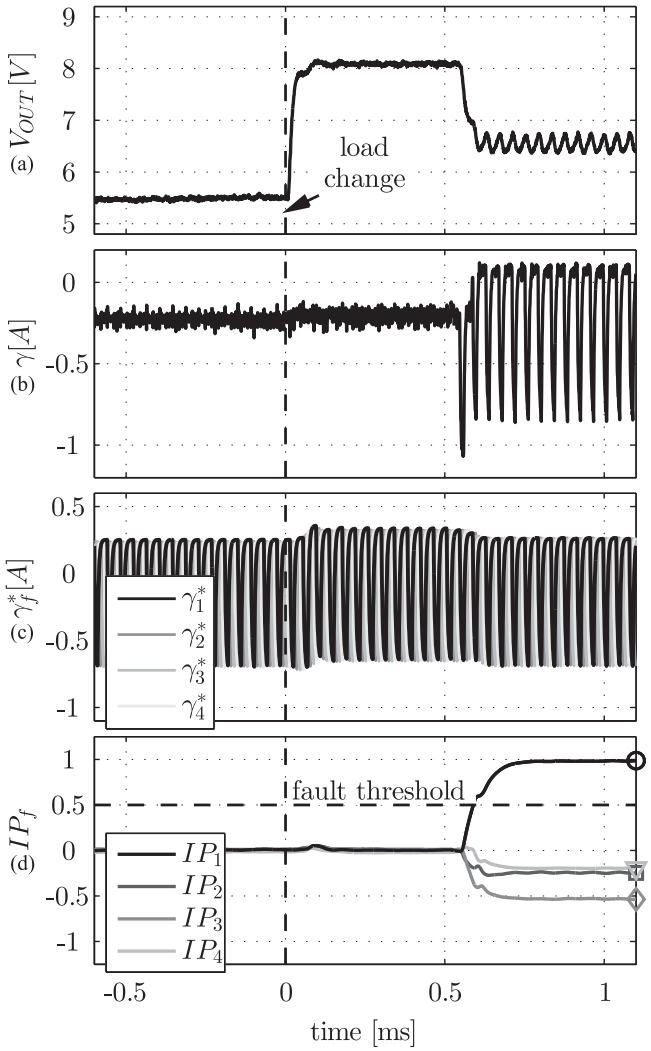

Fig. 12. Relevant signals evolution after a load change. (a) Output voltage. (b) Residual. (c) Fault signatures. (d) Similarity signals.

in Fig. 6, regardless of the D value taken into account, which verifies the selected thresholding strategy.

Below, the robustness of the algorithm to changes in operating conditions is tested. The performance of the identification algorithm under a step change of 100% in the reference at $t = 0$ ms is presented in Fig. 11. Phase 1 current and residual are shown in Fig. 11(a) and (b), respectively. Fault signatures are depicted in Fig. 11(c), where it can be seen how their mean values are readjusted to zero after the reference change. The evolution of different $\mathrm{IP}_f(t)$ is shown in Fig. 11(d), where the transient response after the step in the reference can be noticed. As expected, this transient response is not detected as a fault condition. Additionally, an OCF is evaluated at $t = 0.5$ ms in order to contrast the algorithm performance against both situations. It can be noticed that the algorithm properly detects and identifies the fault state.

A step change of 45% in the load voltage at $t = 0$ ms is evaluated in Fig. 12. Load voltage is displayed in Fig. 12(a), while Fig. 12(b) shows the residual, which exhibits minor variations after load change. Again, the results obtained verify the proper operation of the algorithm in the presence of abrupt changes in the operating conditions. An OCF in phase 1 was evaluated at $t = 0.5$ ms with the same purpose as in the previous test.

V. Conclusion

This paper presents a method for the detection of OCFs in an interleaved power converter. The proposed method identifies the faulty phase from the time information in the residual of a state-space observer, and only requires the measurement of variables commonly used for control schemes (input and output dc-link voltage and total current). It is based on the similarity analysis between the residual and a set of signals representative of the expected faults, with phase information regarding the interleaving operation. In order to quantify similarity, an inner product with a sliding window is used. Moreover, the selection of a window length multiple of the switching period provides rejection to disturbances given by the switching frequency and its harmonics. The evaluation of the signal representing similarity in the whole operating range together with the normalization strategy allowed to define threshold levels intended to achieve robustness against noise, model discrepancies, and other disturbances. Furthermore, a good tradeoff between robustness and identification speed was achieved. The proposed method was experimentally validated on a four-phase interleaved buck prototype, which provides the generation of a controlled OCF event. The experimental results are in good agreement with the theoretical analysis for different operating points, even under model discrepancies. The results obtained for different operating conditions show that the fault identification time is not affected by this situation and that the worst case scenario is close to two switching periods. Additionally, experimental tests with abrupt changes in the reference and the load have proven the robustness of the proposed algorithm.

References

[1] O. Garcia, P. Zumel, A. de Castro, and A. Cobos, "Automotive DC-DC bidirectional converter made with many interleaved buck stages," *IEEE Trans. Power Electron.*, vol. 21, no. 3, pp. 578–586, May 2006.

[2] L. Ni, D. J. Patterson, and J. L. Hudgins, "Maximum power extraction from a small wind turbine using 4-phase interleaved boost converter," in *Proc. IEEE Power Electron. Mach. Wind Appl.*, Jun. 2009, pp. 1–5.

[3] S. V. Dhople, A. Davoudi, A. D. Domínguez-García, and P. L. Chapman, "A unified approach to reliability assessment of multiphase DC-DC converters in photovoltaic energy conversion systems," *IEEE Trans. Power Electron.*, vol. 27, no. 2, pp. 739–751, Feb. 2012.

[4] D. Aguglia, "2 MW active bouncer converter design for long pulse Klystron modulators," in *Proc. 14th Eur. Conf. Power Electron. Appl.*, Aug. 2011, pp. 1–10.

[5] Y. Gu and D. Zhang, "Interleaved boost converter with ripple cancellation network," *IEEE Trans. Power Electron.*, vol. 28, no. 8, pp. 3860–3869, Aug. 2013.

[6] L. Ni, D. J. Patterson, and J. L. Hudgins, "High power current sensorless bidirectional 16-phase interleaved dc-dc converter for hybrid vehicle application," *IEEE Trans. Power Electron.*, vol. 27, no. 3, pp. 1141–1151, Mar. 2012.

[7] P. D. Antoszczuk, R. G. Retegui, N. Wassinger, S. Maestri, M. Funes, and M. Benedetti, "Characterization of steady-state current ripple in interleaved power converters under inductance mismatches," *IEEE Trans. Power Electron.*, vol. 29, no. 4, pp. 1840–1849, Apr. 2014.

[8] E. Ribeiro, A. J. M. Cardoso, and C. Boccaletti, "Open-circuit fault diagnosis in interleaved DC-DC converters," *IEEE Trans. Power Electron.*, vol. 29, no. 6, pp. 3091–3102, Jun. 2014.

[9] P. D. Antoszczuk, R. G. Retegui, M. Funes, and D. Carrica, "Optimized implementation of a current control algorithm for multiphase interleaved power converters," *IEEE Trans. Ind. Informat.*, vol. 10, no. 4, pp. 2224–2232, Nov. 2014.
[10] D. Guilbert, A. N'Diaye, A. Gaillard, and A. Djerdir, "Fuel cell systems reliability and availability enhancement by developing a fast and efficient power switch open-circuit fault detection algorithm in interleaved DC/DC boost converter topologies," *Int. J. Hydrogen Energy*, vol. 41, pp. 15505–15517, Mar. 2016.
[11] M. Shahbazi, E. Jamshidpour, P. Poure, S. Saadate, and M. R. Zolghadri, "Open- and short-circuit switch fault diagnosis for nonisolated DC-DC converters using field programmable gate array," *IEEE Trans. Ind. Electron.*, vol. 60, no. 9, pp. 4136–4146, Sep. 2013.
[12] D. Guilbert, M. Guarisco, A. Gaillard, A. N'Diaye, and A. Djerdir, "FPGA based fault-tolerant control on an interleaved DC/DC boost converter for fuel cell electric vehicle applications," *Int. J. Hydrogen Energy*, vol. 40, no. 45, pp. 15 815–15 822, Dec. 2015.
[13] J. Poon, P. Jain, I. Konstantakopoulos, C. Spanos, S. Panda, and S. Sanders, "Model-based fault detection and identification for switching power converters," *IEEE Trans. Power Electron.*, vol. 32, no. 2, pp. 1419–1430, Feb. 2017.
[14] M. Younsi, M. Bendali, T. Azib, C. Larouci, C. Marchand, and G. Coquery, "Current-sharing control technique of interleaved buck converter for automotive application," in *Proc. 7th IET Int. Conf. Power Electron., Mach. Drives*, Apr. 2014, pp. 1–6, doi: 10.1049/cp.2014.0448.
[15] A. Borrell, M. Castilla, J. Miret, J. Matas, and L. Garcia de Vicuna, "Control design for multiphase synchronous buck converters based on exact constant resistive output impedance," *IEEE Trans. Ind. Electron.*, vol. 60, no. 11, pp. 4920–4929, Nov. 2013.
[16] R. F. Foley, R. C. Kavanagh, and M. G. Egan, "Sensorless current estimation and sharing in multiphase buck converters," *IEEE Trans. Power Electron.*, vol. 27, no. 6, pp. 2936–2946, Jun. 2012.
[17] Y. Cho, A. Koran, H. Miwa, B. York, and J.-S. Lai, "An active current reconstruction and balancing strategy with dc-link current sensing for a multi-phase coupled-inductor converter," *IEEE Trans. Power Electron.*, vol. 27, no. 4, pp. 1697–1705, Apr. 2012.
[18] S. Chae, Y. Song, S. Park, and H. Jeong, "Digital current sharing method for parallel interleaved dc-dc converters using input ripple voltage," *IEEE Trans. Ind. Informat.*, vol. 8, no. 3, pp. 536–544, Aug. 2012.
[19] S.-H. Baek, S.-R. Lee, and C.-Y. Won, "A novel phase shedding control algorithm considering maximum efficiency for 3-phase interleaved boost converter," in *Proc. IEEE Transp. Electrific. Conf. Expo.*, Jun. 2016, pp. 427–431.
[20] Y. Chen, X. Pei, S. Nie, and Y. Kang, "Monitoring and Diagnosis for the dc-dc converter using the magnetic near field waveform," *IEEE Trans. Ind. Electron.*, vol. 58, no. 5, pp. 1634–1647, May 2011.
[21] X. Ding, J. Poon, I. čelanović, and A. D. Domínguez-García, "Fault detection and isolation filters for three-phase AC-DC power electronics systems," *IEEE Trans. Circuits Syst. I, Reg. Papers*, vol. 60, no. 4, pp. 1038–1051, Apr. 2013.
[22] K. T. Levin, E. M. Hope, and A. D. Domínguez-García, "Observer-based fault diagnosis of power electronics systems," in *Proc. IEEE Energy Convers. Congr. Expo.*, Sep. 2010, pp. 4434–4440.
[23] S. Shao, A. J. Watson, J. C. Clare, and P. W. Wheeler, "Robustness analysis and experimental validation of a fault detection and isolation method for the modular multilevel converter," *IEEE Trans. Power Electron.*, vol. 31, no. 5, pp. 3794–3805, May 2016.
[24] X. Hu, J. Zhang, S. Xu, and Y. Jiang, "Fault diagnosis of modular multilevel converters based on extended state observer," in *Proc. IEEE 7th Int. Symp. Power Electron. Distrib. Gener. Syst.*, Jun. 2016, pp. 1–6.
[25] S. Shao, P. W. Wheeler, J. C. Clare, and A. J. Watson, "Fault detection for modular multilevel converters based on sliding mode observer," *IEEE Trans. Power Electron.*, vol. 28, no. 11, pp. 4867–4872, Nov. 2013.
[26] J. Poon *et al.*, "Failsafe: A generalized methodology for converter fault detection, identification, and remediation in nanogrids," in *Proc. IEEE Int. Conf. Building Efficiency Sustain. Technol.*, Aug. 2015, pp. 73–78.
[27] R. Bhattacharya, S. Kumar, and S. Biswas, "Fault diagnosis in switched-linear systems by emulation of behavioral models on FPGA: A case study of current-mode buck converter," in *International Journal of Numerical Modelling: Electronic Networks, Devices and Fields*. Hoboken, NJ, USA: Wiley, 2017, pp. 1–27. [Online]. Available: http://dx.doi.org/10.1002/jnm.2314
[28] D. Liberzon, *Switching in Systems and Control*. Basel, Switzerland: Birkhäuser, 2003.

Nicolas Wassinger was born in Buenos Aires, Argentina, in 1984. He received the electronics engineering degree and Ph.D. degree in engineering from the Universidad Nacional de Mar del Plata (UNMdP), Mar del Plata, Argentina, in 2008 and 2012, respectively.

He is currently a Researcher with the Instrumentation and Control Laboratory (LIC), Institute of Scientific and Technological Research in Electronic, (ICYTE), Buenos Aires, Argentina. Since 2013, he is an Assistant Professor for the Control Systems Course with UNMdP. Since 2014, he has been a Researcher with the National Scientific and Technical Research Council of Argentina (CONICET), Buenos Aires, Argentina. His research interests include power converters, current control, and digital signal processing.

Emiliano Penovi was born in Rosario, Argentina, in 1987. He received the electronics engineering degree and Ph.D. degree in engineering from the Universidad Nacional de Mar del Plata (UNMdP), Mar del Plata, Argentina, in 2011 and 2016, respectively.

Since 2010, he is an Assistant Professor with UNMdP. He is a Researcher with the Instrumentation and Control Laboratory (LIC), Institute of Scientific and Technological Research in Electronic, (ICYTE), Buenos Aires, Argentina. His research interests include power converters, current control, and high-precision measurements.

Rogelio García Retegui was born in Tandil, Argentina, in 1977. He received the electronics engineering degree and Ph.D. degree in engineering from the Universidad Nacional de Mar del Plata (UNMdP), Mar del Plata, Argentina, in 2002 and 2009, respectively.

He is currently a Researcher with the Instrumentation and Control Laboratory (LIC), Institute of Scientific and Technological Research in Electronic, (ICYTE), Buenos Aires, Argentina. Since 2003, he has been an Assistant Professor for the Control Theory and Control Systems Courses with UNMdP. Since 2011, he has been a Researcher with the National Scientific and Technical Research Council (CONICET), Buenos Aires, Argentina. His research interests include power electronics, current control, and pulsed power converters.

Sebastián Maestri was born in Mar del Plata, Argentina, in 1978. He received the electronics engineering degree and Ph.D. degree in engineering from the Universidad Nacional de Mar del Plata (UNMdP), Mar del Plata, Argentina, in 2005 and 2009, respectively.

He is currently a Researcher with the Instrumentation and Control Laboratory (LIC), Institute of Scientific and Technological Research in Electronic, (ICYTE), Buenos Aires, Argentina. Since 2005, he has been an Assistant Professor for the control area with UNMdP. Since 2011, he has been a Researcher with the National Scientific and Technical Research Council (CONICET), Buenos Aires, Argentina. His research interests include power electronics, pulsed power converters for particle accelerators, and line-commutated converters control.